Supporting Information

SI Results and Discussion

Crystal structure of OCP in P1 space group

We made an inadvertent yet striking observation that some OCP-3'hECN crystals turned colorless after a prolonged soaking in a large volume of crystallization buffer. These colorless crystals exhibited poor diffraction despite their large size and sharp edges (Fig. S12a). We managed to collect a crystallographic dataset from one of such crystals that are not completely discolored (Fig. S12b). The X-ray diffraction images from this partially discolored crystal could only be indexed and processed in the P1 space group instead of $P3_221$, despite similar cell dimensions, resulting in six OCP molecules forming three dimers in the unit cell (Table S2). Clearly, the loss of diffraction from the colorless crystals suggests that grossly disordered OCP molecules in the crystal lattice are resulted from the escape of the carotenoid chromophore. Despite the loss of the crystallographic symmetry, the P1 structure obtained from a crystal that retained some red color is similar to the authentic structure indicates that the overall structure of OCP holds well as long as the chromophore remains bound in its cavity (Fig. S5c). If we extrapolate from our captured conformation changes (Figs. 1 and S3), it would explain an opening between two protein domains for the carotenoid to escape.

At a reasonable resolution of 2.3 Å, the P1 structure is well ordered in the protein region, with a small RMSD value of 0.33 Å over the main chain atoms of 290 aligned residues compared to the $P3_221$ structure (Table S1). However, the electron densities are visibly weaker for carotenoids, suggesting partially occupied and/or disordered chromophore (Fig. S5c). The P1 structure shows far less ordered water molecules with a significantly higher average *B*-factor (Table S2 and Fig. S11b). Judging by the *B*-factors, NTD displays higher mobility than CTD, which is consistent to the RMSD matrix of all crystallographic structures of OCP monomers so far (Fig. S9a,c). The long chain carotenoid is also more ordered in CTD, where the β1 ring retains its hydrogen bonds with Tyr201 and Trp288, but with longer donor-acceptor distances compared to the $P3_221$ structure. Some residues exhibit very high *B*-factors (> 60 $Å^2$) including Arg155, Asn156, and Glu244 at the domain interface, the N-terminal extension, the inter-domain linker and Tyr44/Glu118 near the proposed exit tunnel for the carotenoid (Fig. S11b).

SI Materials and Methods

Cloning, expression, purification, and crystallization of OCP-ECN

The OCP-encoding gene *slr1963* from *Synechocystis* PCC 6803 was amplified via polymerase chain reaction (PCR), which was inserted between the NdeI/XhoI sites in the pET30 vector resulting in OCP-pET30 plasmid carrying a 6×His tag at the C-terminus. To promote ECN

incorporation *in vivo*, the OCP-pET30 plasmid was co-expressed in *E. coli* BL21-Gold (DE3) with two other plasmids: the pAC-BETA plasmid containing four beta-carotene-producing genes *CrtB, CrtE, CrtI* and *CrtY* (Addgene plasmid #53272, a gift from Francis X. Cunningham Jr.) and the pBAD LIC vector containing the *CrtO* gene from *Synechocystis* PCC 6803. Site-direct mutagenesis of OCP was carried out according to the standard protocols of QuikChange. The cell culture conditions were based on the published protocols (1) with minor modifications. The *E. coli* cells containing three plasmids grew in TB medium in the presence of kanamycin, ampicillin and chloramphenicol at 37°C until OD_{600} reaches 0.5-0.6. After induction with arabinose (0.02%), the culture continued to grow overnight at 37°C, before further dilution in fresh TB medium with additional arabinose in the following day. When the culture reaches OD_{600} ~1 at 37°C, 0.2 mM IPTG was added to trigger OCP expression. The culture grew at 28°C before harvest.

The cell pellet harvested by centrifugation was re-suspended in lysis buffer (40 mM Tris, 300 mM NaCl, and 10% glycerol at pH 8) using a homogenizer and then subjected to cell lysis by sonication. Following centrifugation, the supernatant was collected, filtered and loaded onto a HisTrap Ni^{2+} column (GE Healthcare). The His-tagged OCP was eluted with 200 mM imidazole. The holo-OCP was further isolated from apo-OCP using size exclusion chromatography and concentrated to 3 mg/ml for crystallization and spectroscopic measurement. The recombinant OCP crystals were obtained under the crystallization condition containing 25% PEG 3350, 0.1 M Bis-Tris (pH 5.5) at room temperature or 15°C incubator using the hanging drop vapor diffusion method.

Expression, purification, and crystallization of OCP-3'hECN

OCP-3'hECN was expressed from a mutant strain of *Synechocystis* PCC 6803, in which the wild-type *ocp* gene is replaced by *ocp-Histag* using the pBlue-ocp-HisTag-kana-arm plasmid via homologous recombination (2). To construct the pBlue-ocp-HisTag-kana-arm plasmid, 954 bp wild-type *ocp* acts as the upstream targeting arm, which was PCR amplified via two primers (5'-atactcgagatgccattcaccattgactct and 5'-attgatatcttaatgatgatgatgatggcgagcaaagttgag) to introduce the C-terminal His tag. The 997 bp segment following *ocp* in the *Synechocystis* genome acts as the downstream targeting arm, which was PCR-amplified using two primers: (5'-cttgatatcaataactcccttcaga and 5'-atcgagctctagtcaaaaactatct). The two DNA segments were subcloned subsequently into the pBluescript plasmid, and finally a DNA segment containing kanamycin resistance cassette was inserted after *ocp-Histag* via the restriction site of *Eco*RV. All constructs have been verified by DNA sequencing.

The mutant expressing OCP-Histag was grown in kanamycin (15 mg/L) containing BG11 medium with a double amount of $NaNO_3$. After harvesting, cell lysis in Tris buffer (with 5 mM EDTA and 0.1 mM PMSF at pH 8) and centrifugation, OCP-Histag was first purified by Ni^{2+}-affinity chromatography and further purified by ion exchange chromatography (HiPrep-Q16/10FF) using a NaCl gradient (buffer A: 40 mM Tris at pH 8; buffer B: 40 mM Tris at pH 8

containing 500 mM NaCl). The purified OCP-Histag was then dialyzed against 10 mM Tris (pH 8) and concentrated to 4.8 mg/mL for crystallization under 100 mM sodium acetate (pH 4.5) containing 16% PEG 8000 and 2% glycerol.

UV/Visible spectroscopy in solution and crystals

UV/Visible absorption spectra of the OCP elution fractions from SEC were measured using Shimadzu UV-2600 spectrophotometer with temperature control. All time series of OCP absorption spectra during photoconversion in solution and in single crystals were recorded by an imaging-based microspectrophotometer developed in our laboratory, which combines a modified Zeiss microscope of 96× magnification and a high-sensitivity spectrometer (QEPro, Ocean Optics). This microspectrophotometer enables direct and accurate measurements of absorption spectra from samples of an optical surface as small as 25 μm.

X-ray data collection and structure determination

All X-ray diffraction data collection was carried out at Sector 21 LS-CAT beamlines of the Advanced Photon Source, Argonne National Laboratory. The crystal structures of both OCP-ECN and OCP-3'hECN was determined in the space group of $P3_221$ by molecular replacement (Phenix/Phaser) (3) using the PDB structure 3MG1 as a search model. The final model contains one OCP molecule in the asymmetric unit. Data collection and refinement statistics are shown in Table S2.

In T-scan experiments, the reference set was collected first at 100 K and the light dataset was then obtained following 10 – 15 minutes illumination (OSL2 illuminator, ThorLabs) under various light conditions (Tables S3 and S4) at elevated cryogenic temperatures 100 – 180 K (CryoJet, Oxford Instruments). The reference and light X-ray datasets were independently processed (HKL2000) (4) before merging (CCP4/CAD) (5) and scaling (CCP4/ScaleIt). The difference Fourier maps were generated using F_{Light}-F_{Dark} as map coefficients with phases calculated from the OCP structure refined against the reference dataset (Fig. S2).

Joint analysis of difference maps

The SVD analyses of difference maps were performed independently for OCP-ECN and OCP-3'hECN using the published method (dynamiX) (6). Briefly, SVD of a data matrix **A** results in $\mathbf{A} = \mathbf{UWV}^{\mathrm{T}}$, where the N columns of the matrix **A** contains difference electron densities from N difference Fourier maps with M grid points each. The matrix **U** of the same shape as **A** contains N decomposed components $\boldsymbol{U}_k$ independent of one another, known as orthonormal left singular vectors. The square matrix **W** contains all zeros except for N positive values on its major diagonal, known as singular values w_k. The magnitude of w_k can be considered as a weight or significance of its corresponding component $\boldsymbol{U}_k$. Each column of the matrix **V** or row of its transpose $\mathbf{V}^{\mathrm{T}}$, known as a right singular vector, contains the relative compositions of the

component $\boldsymbol{U}_k$. Each difference Fourier map is therefore expressed as a linear combination of $\boldsymbol{U}_k$, for example, the j-th map is decomposed into $w_1v_{j1}\boldsymbol{U}_1 + w_2v_{j2}\boldsymbol{U}_2 + w_3v_{j3}\boldsymbol{U}_3 + \ldots$, where w_kv_{jk} or $w_k\boldsymbol{V}_k$ is the coefficient set for the linear combination. A singular triplet denotes 1) a decomposed component $\boldsymbol{U}_k$, 2) its singular value w_k, and 3) the composition function $\boldsymbol{V}_k$. Singular triplets are often sorted in a descending order of their singular values w_k. Only a small number of n most significant singular triplets identified by the greatest singular values $w_1 - w_n$ can be used in an abbreviated linear combination to reconstruct a difference Fourier map that closely resembles the original one, where $n < N$. As a result, the structural information evenly distributed in all original difference maps is effectively concentrated into the n most significant components. In the meantime, the inconsistent fluctuations in the original maps are decomposed into the higher order thus less significant components that can be readily eliminated. Last but not least, systematic errors such as the effect of radiation damage and varying density features due to uneven resolution from one dataset to another can also be decomposed into independent components so that these errors can be corrected or evened up (6).

In each collection of difference maps (Tables S3 and S4), the first decomposed component stands out judging by the singular values w_k (Fig. 1f). The second and third components show no clear correlation with light or temperature conditions, and they may arise from the individualities from crystal to crystal. The top component of each collection constitutes a noise-filtered difference map extracting the major and consistent map features among the experimental maps in each collection.

Real space refinement against difference maps

Structural refinement in both reciprocal and real space was carried out to characterize these difference signals in a quantitative manner (Fig. S2). A starting model of the light structure was first obtained by refining the reference structure against a set of extrapolated structure amplitudes (phenix.refine)(3). For example, if we assume that 20% of molecules in a crystal enter the reaction, the extrapolated light dataset was produced by adding five times of the difference structure factor amplitude i.e. $5 \times (F_{\text{Light}}\text{-}F_{\text{Dark}})$ to the amplitudes of the reference dataset. The resulting "light" coordinates and the reference structure are then used as the starting models in a simultaneous refinement in real space against the first component produced by SVD, that is, an SVD-filtered difference map, to achieve the best agreement between the calculated and observed difference densities (Fig. 2h,i). In contrast to conventional real space refinement against an electron density map, real space refinement against a difference map is less straightforward. While atoms are displaced away from negative difference densities to positive densities, they shall not be centered on the positive peaks. A general strategy is to iteratively adjust the coordinates under certain stereochemical restraints while minimizing the discrepancy between the target difference map and the theoretically calculated difference map (6). The difference map calculation from the refined models is carried out using CCP4 (5).

SI Tables

Table S1. Comparisons of the OCP crystal structures

PDB entry	5TUX	5TV0[1]	5TUW[2]	1M98[1]	3MG1	3MG2	3MG3	4XB5	5HGR
Source organism	*Synechocystis* PCC 6803 (this work)			*Arthrospira maxima*	*Synechocystis* PCC 6803				*Anabaena* PCC 7120
Protein	Wild types					Y44S	R155L	Wild type	Wild type
Pigment	ECN	3'hECN			ECN			CAN	CAN
Crystallization condition									
Buffer/pH	BisTris/5.5	NaAc/4.5		Tris/7.7	NaAc/5		NaAc/4.8	NaAc/4.5	Na formate/6
Precipitant	PEG 3350	PEG 8000		PEG 3350	PEG 4000		PEG 3350	PEG 20000	PEG 3350
Salt/other	-	2% glycerol		NaCl	-	2% glycerol		3% glycerol	-
Space group	$P3_221$		P1	C2	$P3_2$			$P3_221$	P1
Asymmetric unit content	Monomer		3 dimers	Dimer				Monomer	Dimer
Resolution (Å)	1.5	1.65	2.3	2.1	1.65	2.65	1.7	1.9	1.68
Cell parameters									
a (Å)	82.29	82.64	82.95	217.2	82.94	83.12	82.68	82.89	52.99
b (Å)	82.29	82.64	82.92	40.76	82.94	83.12	82.68	82.89	53.37
c (Å)	87.68	88.01	87.44	75.46	87.63	87.97	86.57	87.2	65.04
α (°)	90	90	89.79	90	90	90	90	90	83.23
β (°)	90	90	89.91	95.9	90	90	90	90	112.93
γ (°)	120	120	60.04	90	120	120	120	120	93.09
RMSD (Å)	Reference	0.148	0.330	0.627	0.127	0.199	0.188	0.286	0.577

[1]Our high-resolution structure of OCP-3'hECN from *Synechocystis* PCC 6803 shows an R-configuration at 3'-C position in the β2 ionone ring in contrast to the S-configuration at the equivalent position in the OCP-3'hECN structure from *Anthrospira maxima*. PDB ID 1M98 has been recently updated with a new PDB ID 5UI2.

[2]Soaked in well solution for 2 months.

Table S2. Statistics of data collection and structure refinement

Structure	OCP-ECN	OCP-3'hECN	OCP-3'hECN
Space group	$P3_221$	$P3_221$	P1
Cell parameters			
a, *b*, *c* (Å)	82.5, 82.5, 87.8	82.9, 82.9, 86.9	82.95, 82.91, 87.44
α, β, γ (°)	90, 90, 120	90, 90, 120	89.79, 89.91, 60.04
Asymmetric unit content			
Residues	2-314 (1 OCP)	2-314 (1 OCP)	2-314 (6 OCPs)
Waters	374	245	263
Ligands	1 ECN, 1 glycerol, 1 Cl^-	1 3'hECN, 1 glycerol, 1 Cl^-	6 3'hECNs
Diffraction data			
X-ray source	21-ID-F, APS	21-I-D-G, APS	21-ID-D, APS
Resolution (Å)	50-1.5 (1.53-1.5)[1]	50-1.65 (1.68-1.65)	50-2.3 (2.36-2.3)
R_{merge}	0.041 (0.408)	0.034 (0.512)	0.102 (0.52)
Completeness (%)	95 (63)	99.9 (99.9)	96 (89.9)
Redundancy	4.9 (2.2)	5.4 (3.9)	1.9 (1.6)
$I/\sigma(I)$	23.9 (2.0)	27 (1.83)	11 (1.0)
Refinement			
Resolution (Å)	37.41-1.5 (1.53-1.5)	37.4-1.65 (1.69-1.65)	41.5-2.3 (2.36-2.3)
R	0.161 (0.223)	0.177 (0.301)	0.185 (0.295)
R_{free}	0.183 (0.234)	0.203 (0.321)	0.239 (0.335)
RMSD			
Bond length (Å)	0.006	0.007	0.009
Bond angle (°)	0.775	0.971	1.013
Average *B* ($Å^2$)	13.08	21.22	42.41
Ramachandran			
Favored (%)	99.4	98.3	98.6
Allowed (%)	0.6	1.7	1.4
Disallowed (%)	0	0	0
PDB ID	5TUX	5TV0	5TUW

[1]Highest resolution shell in parentheses

Table S3. Data statistics of T-scan experiments in OCP-3h'ECN crystals

Crystal	R_{merge}		R_{diff}	Completeness	Resolution	Illumination[1]	Temperature
	Dark	Light		(%)	(Å)		(K)
117	0.056	0.073	0.075	99.7	1.8	Flooded white light	150
115	0.047	0.066	0.190	99.0	2.1	Flooded white light	180
215	0.032	0.032	0.020	100.0	1.75	Focused (450 ± 30 nm)	100
127	0.045	0.046	0.038	100.0	1.8	Focused (450 ± 30 nm)	130
124	0.052	0.050	0.056	99.2	1.7	Focused (450 ± 30 nm)	130
121	0.051	0.055	0.071	97.7	1.76	Focused (450 ± 30 nm)	150
133	0.048	0.040	0.075	99.7	1.8	Focused (450 ± 30 nm)	160
126	0.039	0.043	0.101	96.8	1.65	Focused (450 ± 30 nm)	170
126	0.067	0.052	0.131	92.6	1.65	Focused (450 ± 30 nm)	180
125	0.037	0.038	0.131	92.9	1.8	Focused (450 ± 30 nm)	180
131	0.045	0.043	0.101	99.2	1.8	Ambient light	170
137	0.040	0.041	0.112	99.5	1.8	Ambient light	170
129	0.035	0.036	0.057	99.8	1.7	Ambient light	100
138	0.034	0.034	0.047	99.9	1.65	Ambient light	100
122	0.044	0.044	0.058	99.9	1.85	Focused white light	100
123	0.047	0.048	0.098	99.7	1.8	Focused white light	130
2310	0.069	0.055	0.055	93.5	2	Focused white light	150
2210	0.090	0.066	0.073	99.4	2	Focused white light	170
129	0.027	0.027	0.058	97.9	1.9	Continuous white light[2]	100

[1]Photosynthetic photon flux (PPF; μmol photons m^{-2} s^{-1}): focused white light 3.5×10^4; flooded white light 2×10^3; focused blue light at 450 ± 30 nm 6.5×10^2; ambient light 7

[2]Flooded white light continuously on during data collection

Table S4. Data statistics of T-scan experiments on OCP-ECN crystals

Crystal	R_{merge}		R_{diff}	Completeness	Resolution	Illumination[1]	Temperature
	Dark	Light		(%)	(Å)		(K)
137	0.043	0.037	0.081	99.7	1.7	Focused (450 ± 30 nm)	170
136	0.043	0.037	0.039	94.6	1.6	Focused white light	100
228	0.041	0.035	0.038	95.0	1.5	Focused white light	130
136	0.043	0.043	0.082	97.6	1.6	Focused white light	150
229	0.034	0.034	0.067	90.4	1.5	Focused white light	150
228	0.041	0.035	0.075	95.0	1.5	Focused white light	170
136	0.042	0.044	0.101	99.9	1.65	Ambient light	150
137	0.042	0.039	0.094	99.9	1.6	Ambient light	170
139	0.054	0.060	0.073	97.5	1.7	Ambient light	150
134	0.051	0.045	0.101	95.6	1.6	Ambient light	170
1310	0.048	0.067	0.069	99.1	1.7	Ambient light	100
135	0.052	0.036	0.068	99.6	1.7	Ambient light	130
236	0.032	0.040	0.048	99.8	1.8	Ambient light	100
239	0.166	0.035	0.091	99.2	1.8	Ambient light	150
137	0.043	0.037	0.091	99.7	1.75	Focused (450 ± 30 nm)	170
2210	0.090	0.066	0.076	99.4	2.1	Focused white light	170
111	0.057	0.038	0.052	99.8	1.9	Continuous white light[3]	100
216	-[2]	0.060	-[2]	98.6	1.7	Focused white light	293
133	-[2]	0.047	-[2]	100.0	1.8	Focused white light	293
2110	-[2]	0.055	-[2]	92.9	1.7	Focused white light	293

[1]Photosynthetic photon flux (PPF; μmol photons m^{-2} s^{-1}): focused white light 3.5×10^4; flooded white light 2×10^3; focused blue light at 450 ± 30 nm 6.5×10^2; ambient light 7

[2]No dark dataset can be collected from the same crystal, if the crystal is illuminated at room temperature. Only a light dataset is collected.

[3]Flooded white light continuously on during data collection

SI Figures and Legends

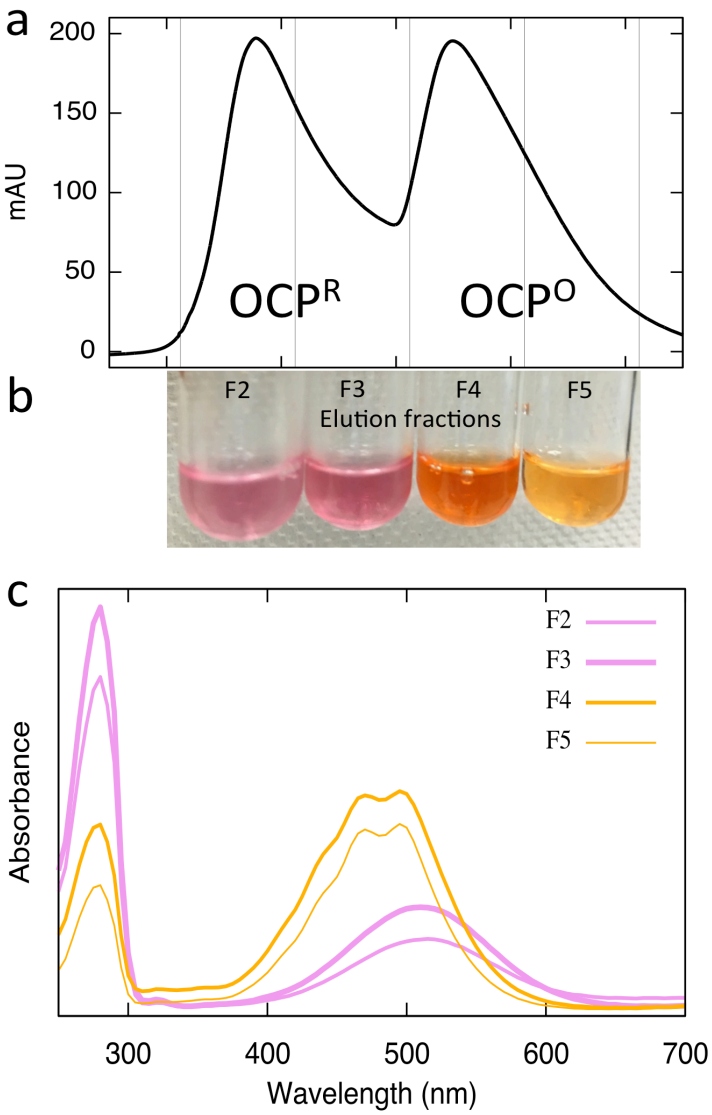

Figure S1. Size exclusion chromatography of illuminated OCP samples. The mixed sample of holo-OCP and apo-OCP at a concentration of 1 mg/mL was illuminated on ice before loading into the sizing column (GE Superdex 200). The elution profile (**a**) and distinct colors (**b**) of the elution fractions indicate clear separation of OCP^R and OCP^O. **c)** Absorption spectra of the elution fractions. That the A_{500}:A_{280} ratios in the fraction F2 and F3 are far less than those of F4 and F5 is not due to loss of chromophore in OCP^R, rather it is attributed to co-migration of apo-OCP and OCP^R, which have similar hydrodynamic properties.

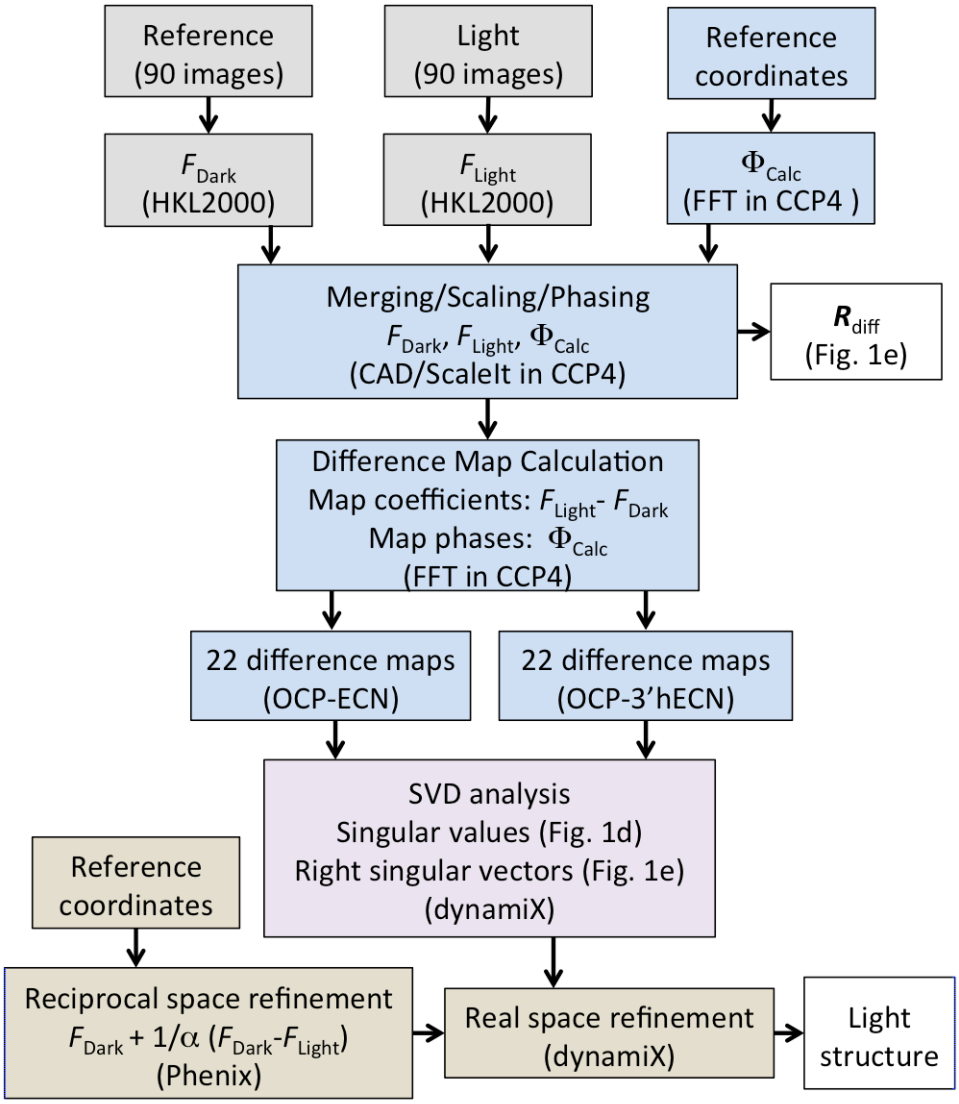

Figure S2. Workflow of the dynamic crystallography method. This flowchart summarizes the methods of collection and processing of diffraction data (gray), difference map calculation (blue), SVD analysis (purple), and structure refinement in reciprocal space and real space (yellow). The protocols and software packages used are indicated in parentheses.

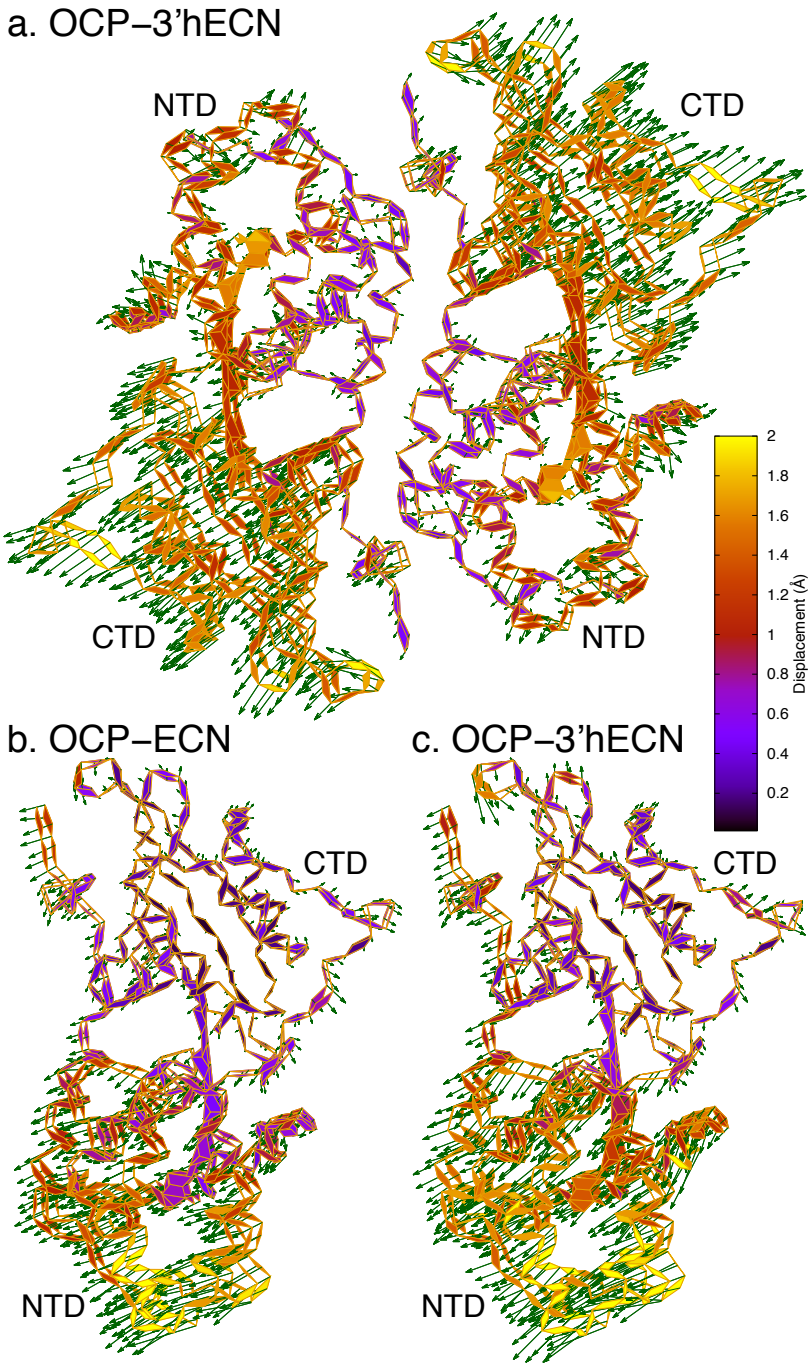

Figure S3. Structural motions refined against the difference electron density maps. Green arrows mark the directions and amplitudes (3×) of the light-induced structural motions. **a)** The dimer of OCP-3'hECN in comparison with OCP-ECN shown in Fig. 1d. **b-c)** Alignment of the dark and light structures according to the rigid core of CTD (Fig. S9a,c) reveals the motions in NTD and the N-terminal extension relative to the rigid CTD core.

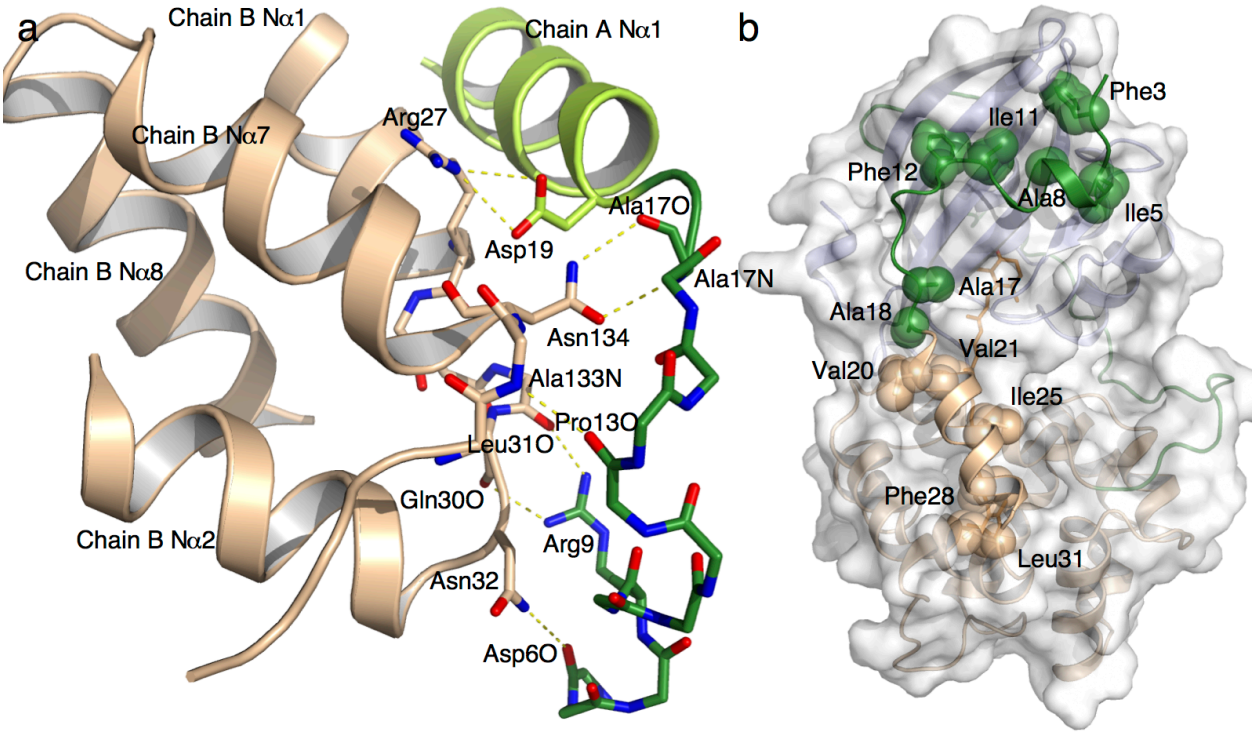

Figure S4. Molecular environment of the N-terminal extension (NTE) in the OCP dimer. **a)** At the dimer interface, NTE (green stick model) and the helix Nα1 (in yellow green) of chain A form extensive interactions (shown in dashed lines) with NTD of the partner subunit B (in light brown stick and ribbon model). **b)** In the same subunit, NTE (green) and helix Nα1 (light brown) are packed against the CTD and NTD core domains, respectively (rendered in white surface) via hydrophobic side chains labeled and rendered in spheres.

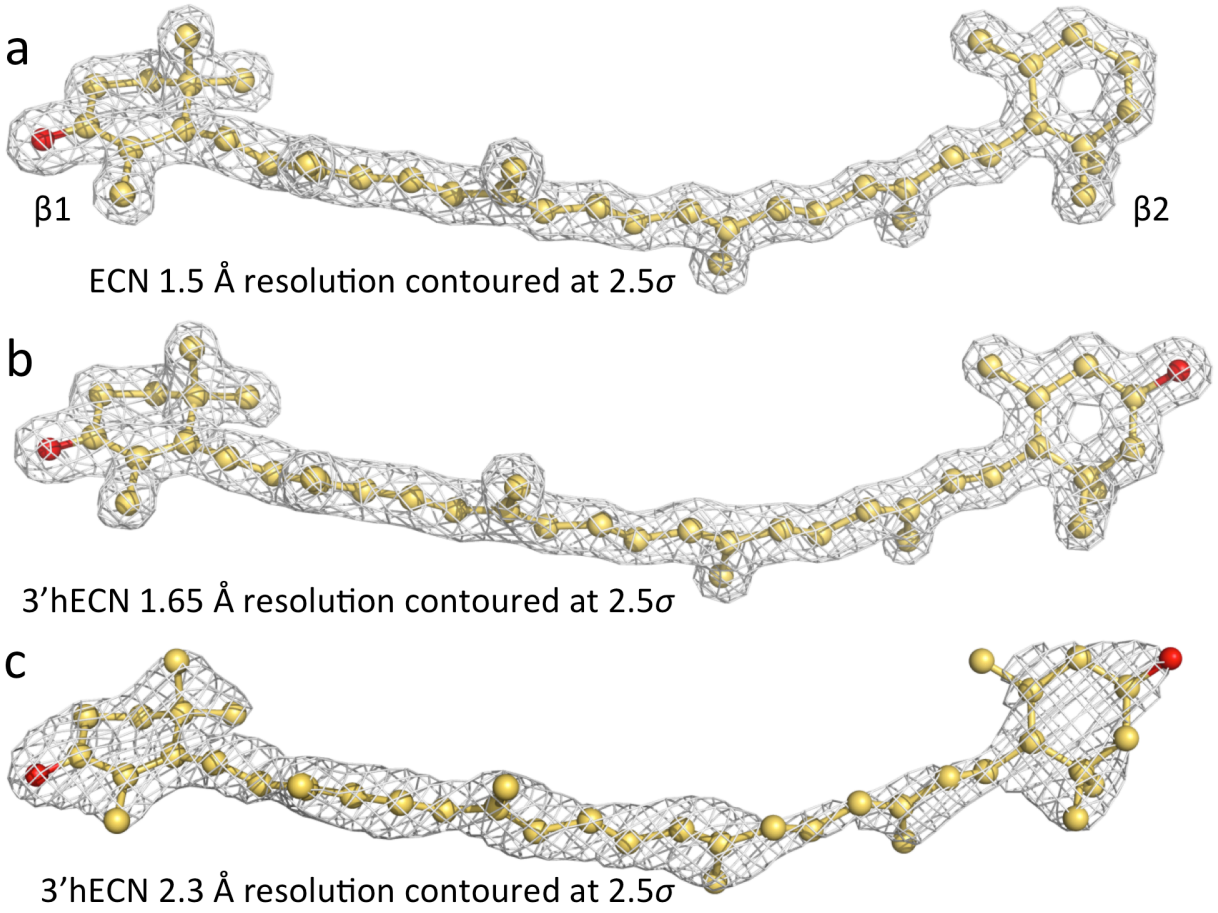

Figure S5. 2*Fo*-*Fc* maps of ketocarotenoids in the three structures presented in this work. **a)** OCP-ECN in the $P3_221$ space group; b) OCP-3'hECN in the $P3_221$ space group; **c)** OCP-3'hECN in the P1 space group (Table S2).

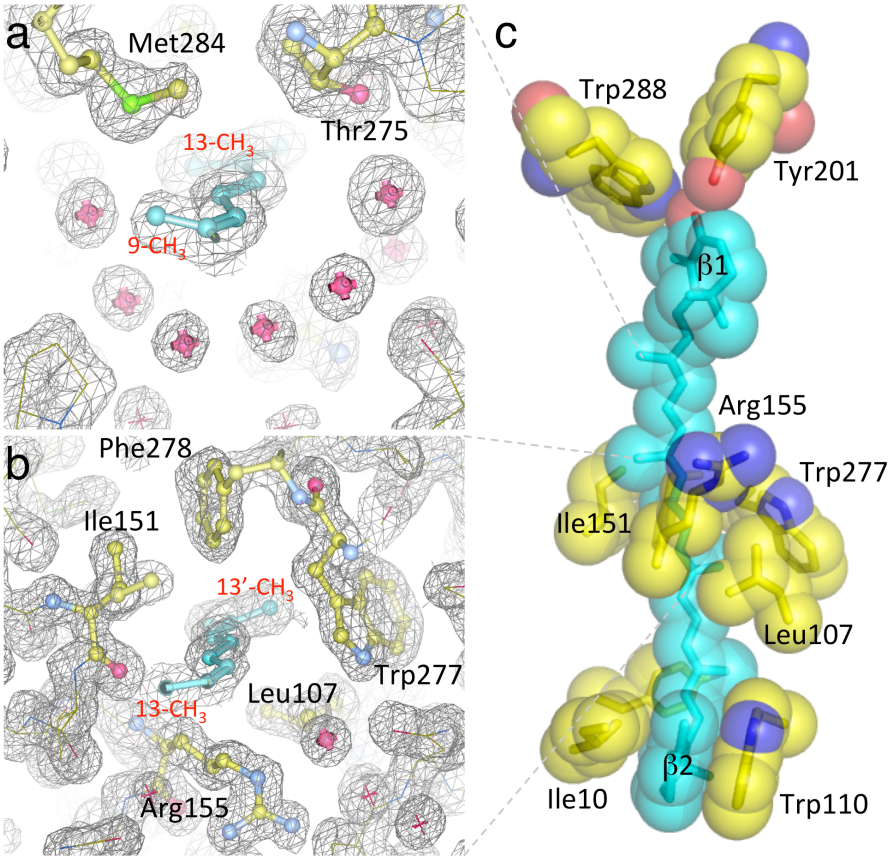

Figure S6. Protein environment of the chromophpre. **a)** The 2*F*o-*F*c map contoured at 1.5σ shows that the cavity around the C9-C13 segment of the ketocarotenoid (cyan) is filled with well-ordered water molecules (in red crosses). **b)** The C13-C13' segment of the ketocarotenoid is closely surrounded by residues colored in yellow. **c)** A space-filling model shows key interactions between the protein and carotenoid in the OCP^{O} structure.

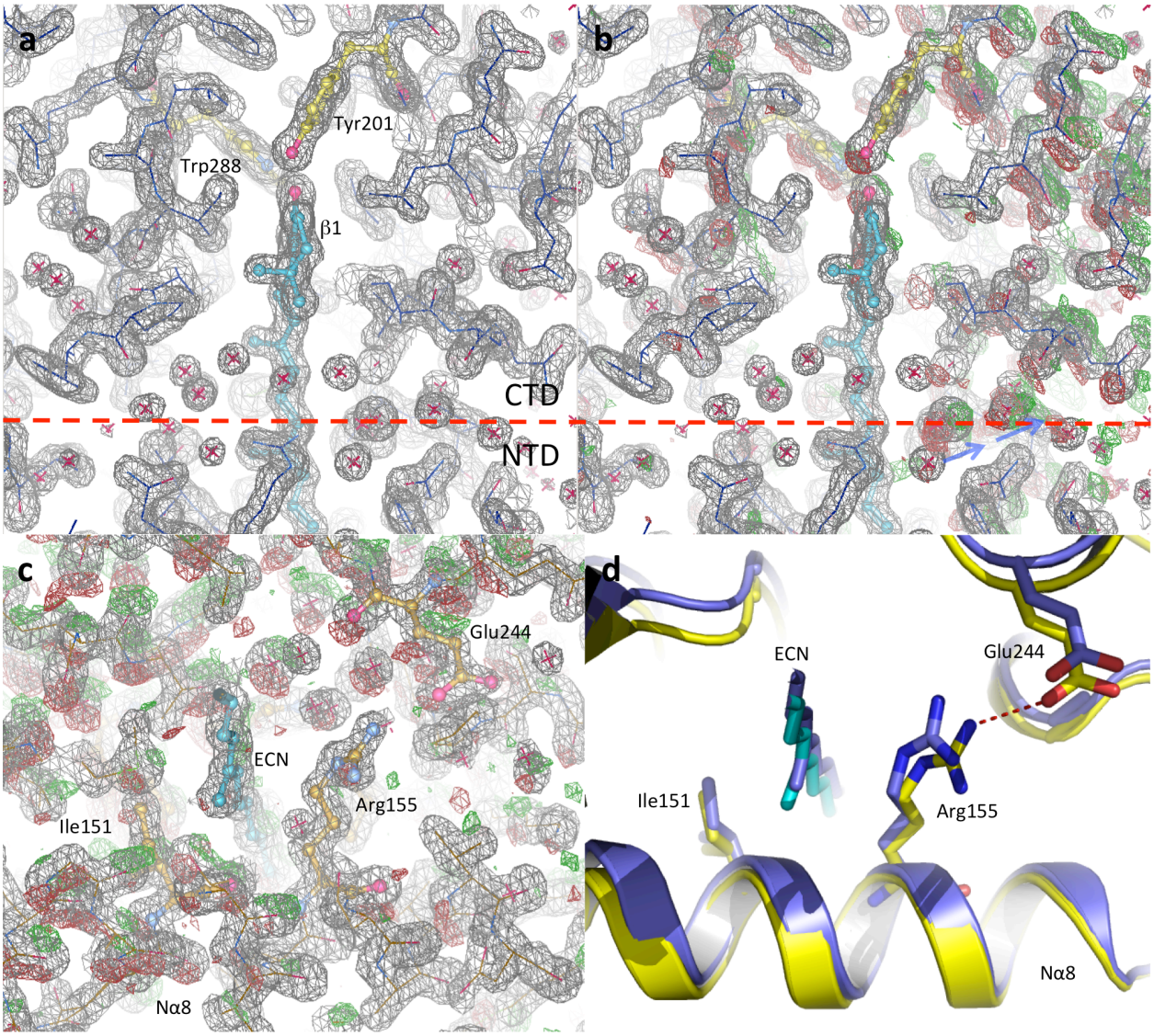

Fig. S7. Structural changes at the NTD-CTD domain interface. a) 2*F*o-*F*c map contoured at 1.5σ shows a network of well-ordered water molecules at the NTD-CTD interface marked by dashed red line. This view is similar to that in Fig. 1c,d. **b)** The F_{Light}-F_{Dark} difference map superimposed on **a** reveals that some water molecules move along with CTD as indicated by blue arrows. Positive and negative densities are contoured ±2.5σ in green and red, respectively. **c)** The difference map (green and red) and 2*F*o-*F*c map (gray) show that helix Nα8 in close contact with the ketocarotenoid (cyan) is slightly distorted due to the differential movements in two helical segments. **d)** At the domain interface, the salt bridge between Arg155 and Glu244 in the reference structure (yellow) is disrupted in the light structure (blue).

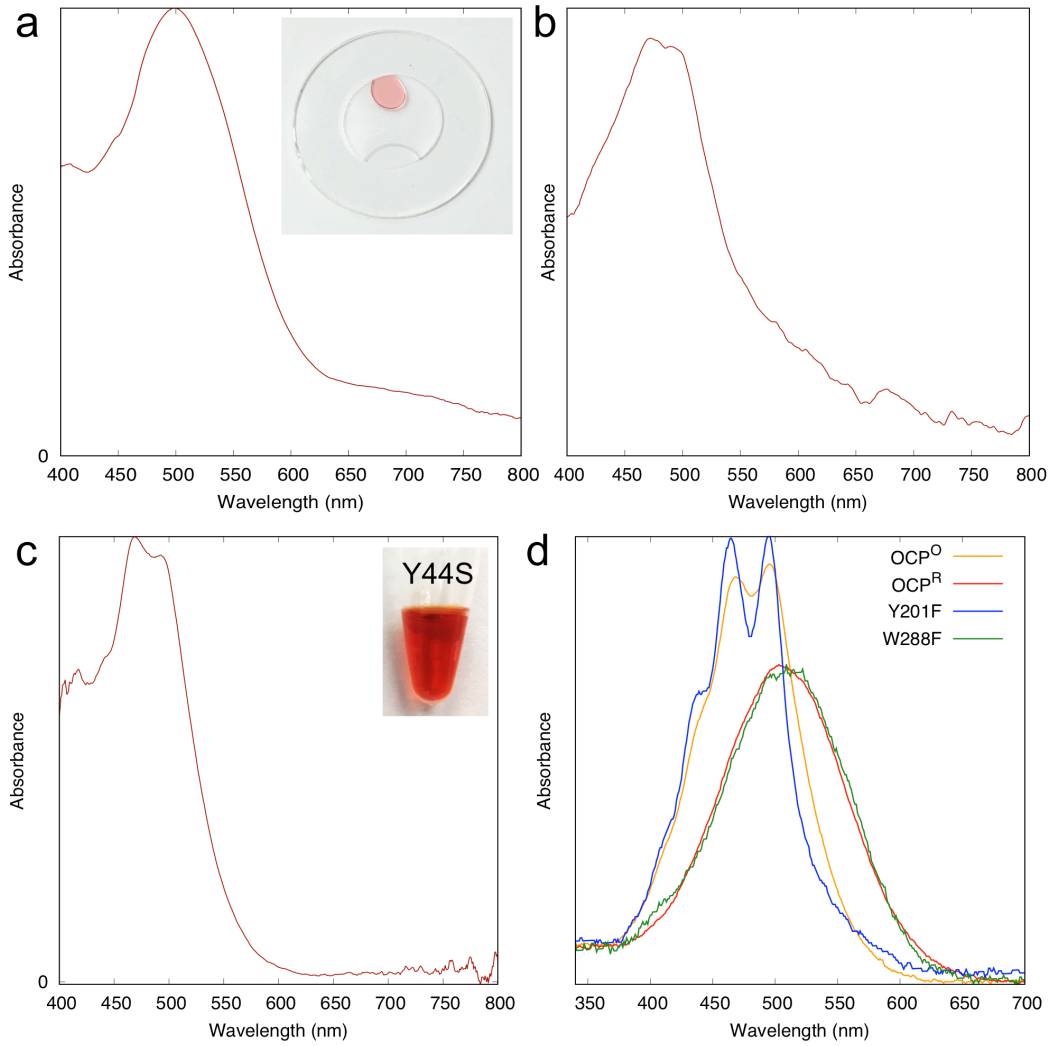

Figure S8. Absorption spectra of OCP under different conditions. a) Absorption spectrum from the same sample after exposure to ambient light for ~3 weeks. **b)** Absorption spectrum of OCP re-solubilized from the aged crystals. **c)** Absorption spectrum of the Y44S mutant. No light-induced spectral change is observed. **d)** Comparison of absorption spectra from OCP^O, OCP^R, and mutants in solutions.

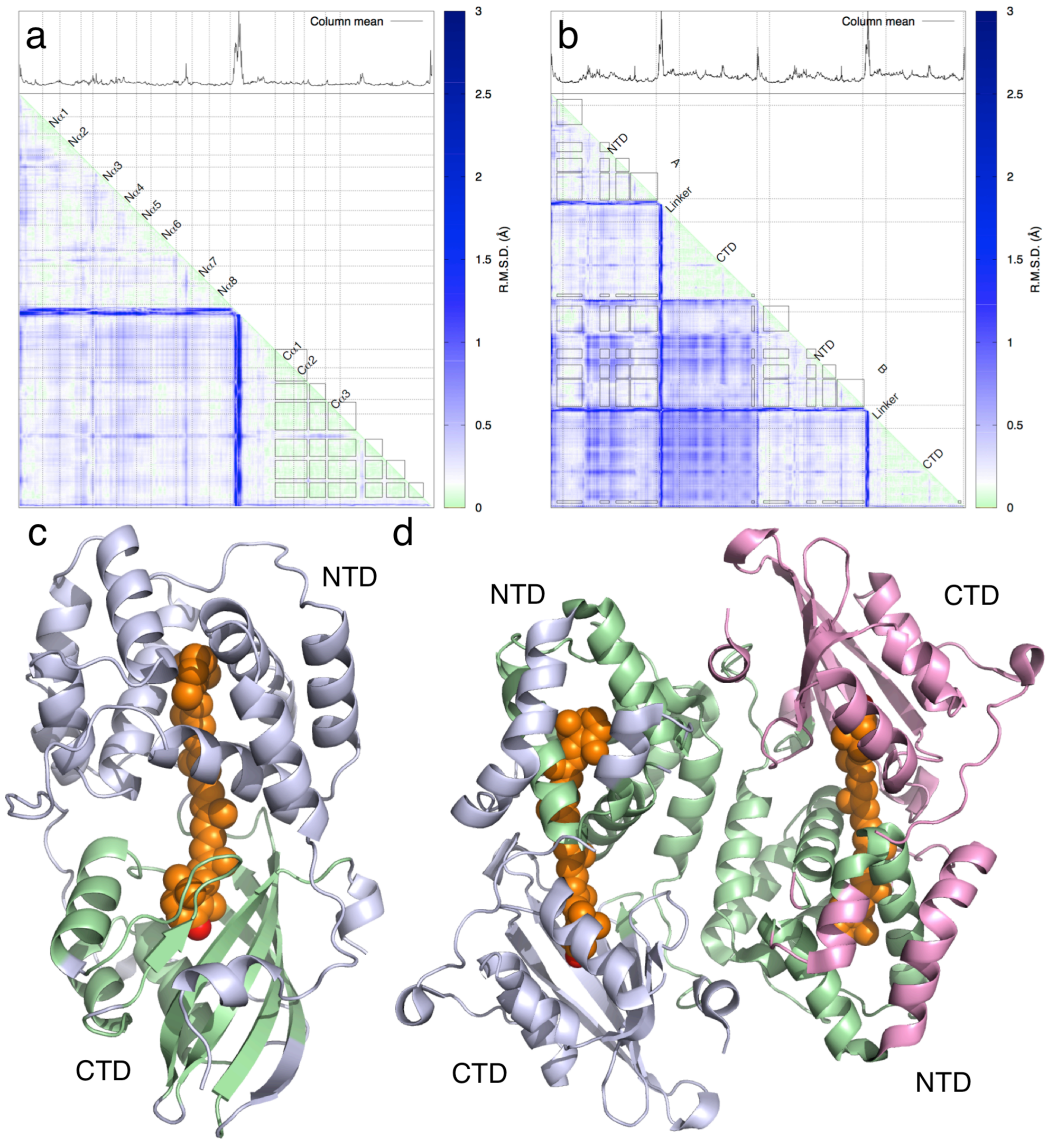

Figure S9. Rigid structural framework of OCP. RMSD of the interatomic distance matrices (7, 8) can be used to identify the rigid protein framework. The RMSD distance matrices of the OCP monomer (**a**) and dimer (**b**) structures are calculated from all available structures of OCP (Table S1). The submatrices of small RMSD values (green/white areas outlined by solid rectangles) indicate regions with minimal structural variations. In the OCP monomer, CTD is relatively more rigid than NTD. The rigid core of CTD (colored in green in **c)** includes residues 195-219, 221-233, 235-256, 263-276, 279-293, and 296-307. The average RMSD value among 23 independently determined OCP monomers is only 0.106 Å within the rigid core of CTD. In contrast, the interatomic distances between two CTDs of the same dimer vary significantly (**b**). The regions of NTD showing the smallest RMSD values include residues 10-48, 75-89, 99-162, and a few residues near the C-terminus 304-308 (green in **d**). The average RMSD within the boxed small-value submatrices is 0.203 Å.

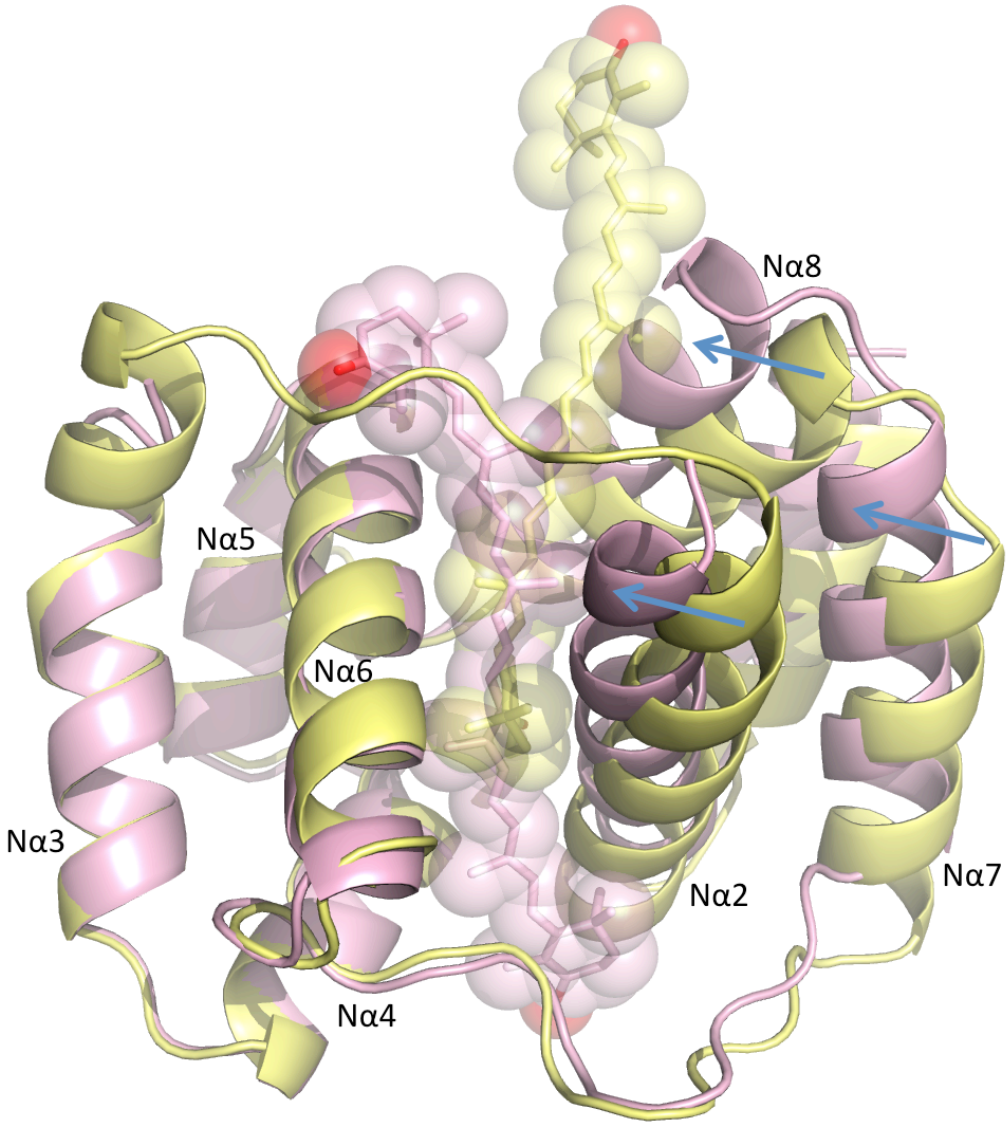

Figure S10. Structural comparison between OCP and RCP in NTD. Structural alignment between OCP (PDB ID 4XB5; yellow) and RCP (PDB ID 4XB4; pink) is based on the rigid framework of the four-helical bundle consisting of Nα3-6 in NTD. The other four-helix bundle of NTD consisting of Nα1/2 and Nα7/8 is displaced significantly to accommodate the carotenoid that is closely associated with the protein moiety in RCP as indicated by blue arrows.

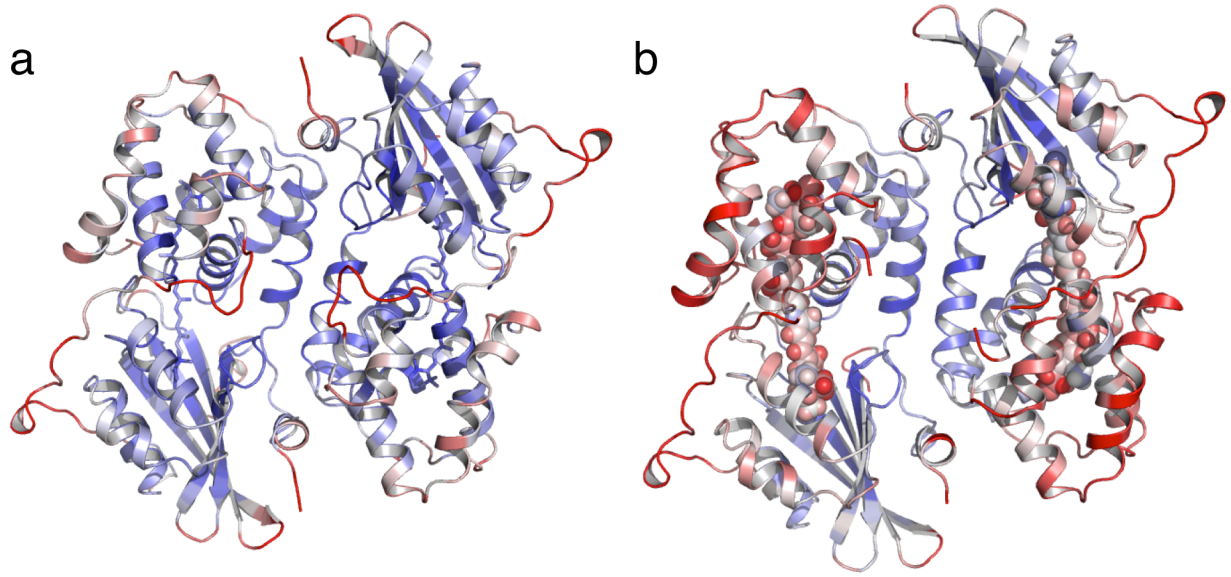

Figure S11. *B*-factor distribution. The OCP structure is colored from blue to white to red according to the ascending order of temperature factor *B*. **a)** The OCP-3'hECN dimer in the $P3_221$ space group exhibits temperature factors ranging from 10 to 30 $Å^2$. **b)** The OCP-3'hECN dimer in the P1 space group is colored based on the temperature factors ranging from 20 to 80 $Å^2$.

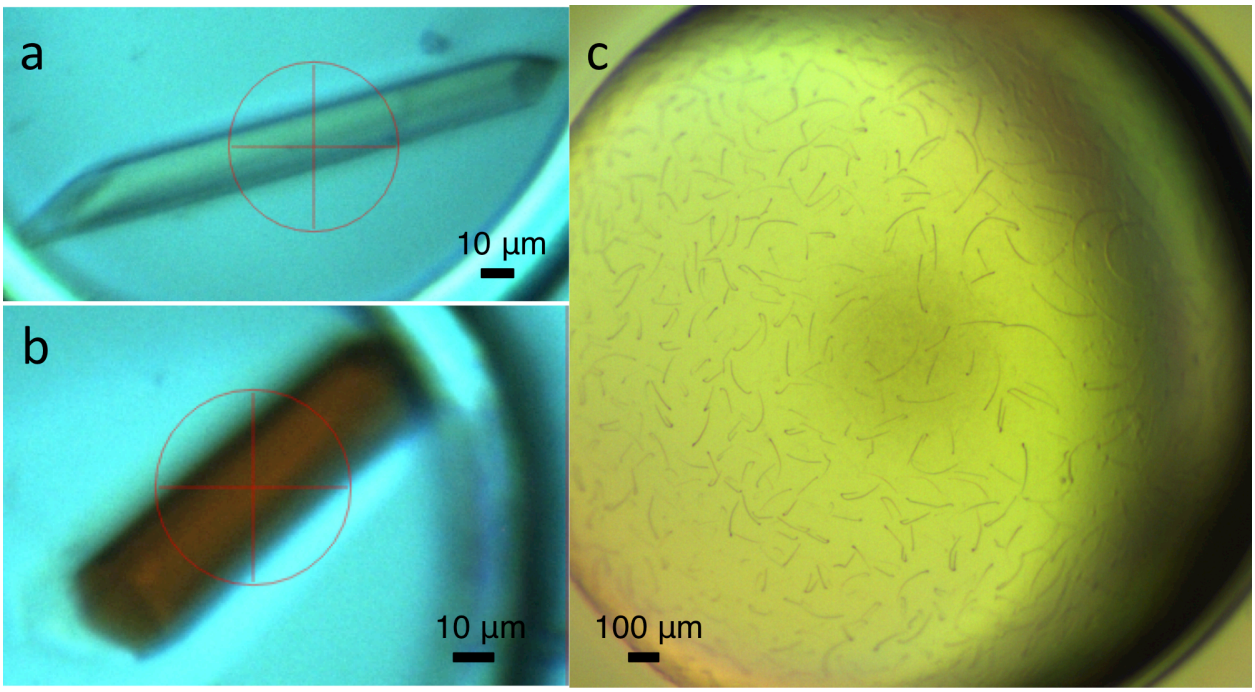

Figure S12. OCP crystals under various conditions. **a)** A colorless crystal of OCP-3'hECN after 1-2 months soaking in a large reservoir of crystallization buffer indicates loss of pigment. Such colorless crystals, despite their good morphology, completely lost the Bragg diffraction. **b)** A partially discolored OCP-3'hECN crystal. A crystal with partial pigment loss diffracted to 2.3 Å resolution in P1 space group (Table S2). **c)** Curved OCP-ECN crystals after extended exposure to room light. Aged thin crystals curled up in the original crystallization drop.

SI References

1. de Carbon CB, Thurotte A, Wilson A, Perreau F, Kirilovsky D (2015) Biosynthesis of soluble carotenoid holoproteins in Escherichia coli. *Sci Rep* 5:9085.

2. Golden SS, Brusslan J, Haselkorn R (1987) Genetic engineering of the cyanobacterial chromosome. *Methods in Enzymology* (Elsevier), pp 215–231.

3. Adams PD, et al. (2010) PHENIX: a comprehensive Python-based system for macromolecular structure solution. *Acta Crystallogr D Biol Crystallogr* 66(2):213–221.

4. Otwinowski Z, Minor W (1997) [20] Processing of X-ray diffraction data collected in oscillation mode. *Methods in Enzymology*, Macromolecular Crystallography Part A., ed Charles W. Carter J (Academic Press), pp 307–326.

5. Winn MD, et al. (2011) Overview of the CCP4 suite and current developments. *Acta Crystallogr D Biol Crystallogr* 67(4):235–242.

6. Ren Z, et al. (2013) Resolution of structural heterogeneity in dynamic crystallography. *Acta Crystallogr Sect D* 69(6):946–959.

7. Ren Z (2013) Reaction trajectory revealed by a joint analysis of Protein Data Bank. *PLoS ONE* 8(11):e77141.

8. Ren Z (2016) Molecular events during translocation and proofreading extracted from 200 static structures of DNA polymerase. *Nucleic Acids Res* 6(43129):1–13.